Journal of Applied Fluid Mechanics, Vol. 18, No. 2, pp. 450-467, 2025.
Available online at www.jafmonline.net, ISSN 1735-3572, EISSN 1735-3645.
https://doi.org/10.47176/jafm.18.2.2791

Numerical Modal Analysis of the Correlation Between Spanwise Vortex Shedding and Far-field Aeolian Noise for Square and Circular Wall-mounted Cylinders

R. P. Jiang[1, 2], P. Q. Liu[1,2], J. Zhang[3†] and H. Guo[1,2]

[1] *Key Laboratory of Aero-Acoustics of Ministry of Industry and Information Technology, Beihang University, Beijing 100191, China*
[2] *School of Aeronautic Science and Engineering, Beihang University, Beijing 100191, China*
[3] *Sino-French Engineer School, Beihang University, Beijing 100191, China*

†*Corresponding Author Email: jin_zhang@buaa.edu.cn*

ABSTRACT

For square and circular finite wall-mounted cylinders (FWMCs) with an aspect ratio exceeding 10, the vortex shedding near the tip area leads to the generation of multiple tonal noises. The quantitative analysis of the spanwise distributions of the vortex modal energy with different frequencies was quite limited. This study employs dynamic mode decomposition to decompose the wake of FWMC into distinct frequencies to evaluate the modal energy distribution of pressure fluctuations at each frequency along the spanwise direction. Large eddy simulation combined with the Ffowcs Williams–Hawkings (FW–H) acoustics analogy is applied to a square and a circular FWMC with aspect ratio of 13.6 at a Reynolds number of 2.3×10^4. Two indicators to describe the spanwise energy contribution are proposed. The results reveal that, for square FWMC, the primary modal energy corresponding to Strouhal number (St) equal to 0.14 is concentrated below 30% of the cylinder height L owing to the 3D effect. A transition mode of $St \approx 0.12$ is identified in the midspan (0.3 L–0.7 L) without significant contribution to far-field noise spectrum. For circular FWMC, the modal energy is distributed over several frequencies, vortices cells corresponding to the main noise band ($0.2 < St < 0.23$) are distributed below 0.7 L, and the vortices cells in the noise band of $0.15 < St < 0.19$ distributed from the midspan to the upper part in a dispersed manner. The noise band with $St \approx 0.08$ corresponds to tip-associated vortices gathering above $0.8L$.

Article History

Received April 25, 2024
Revised August 17, 2024
Accepted August 29, 2024
Available online December 4, 2024

Keywords:

Aeroacoustics
Finite wall-mounted cylinder
Dynamic mode decomposition
Spanwise energy distribution
Modal energy contribution

1. INTRODUCTION

The finite wall-mounted cylinder (FWMC) is a common model utilized in scientific research and industrial applications. FWMC will generate complex aerodynamic and aeroacoustic phenomena with significant 3D effects. Attachments on the ground or various structures like ships, high-speed trains, and aircraft, including wind turbine prop, chimneys, antennas, pantographs, and pitot tubes, probably generate aeolian noise and vibration as a result of strong winds or high-speed motion. Quantitative analysis of the correlation between vortex shedding frequencies at different positions in the wake of these structures and far field noise is quite necessary in revealing the aeroacoustic noise generation mechanism in various engineering disciplines, such as environmental engineering and aviation.

The main phenomenon of an infinite length cylinder is the alternate shedding of vortices with an antisymmetric vorticity and pressure distribution pattern, known as the von Karman vortex street. This phenomenon is 2D, quasi-periodic, and uniform across the span of the cylinder (Inoue & Hatakeyama, 2002). In the case of a tall FWMC, the von Karman vortex street is affected by horseshoe vortices at the intersection of the cylinder and the wall plane, as well as the downward flow from the free end (or tip) of the cylinder (Wang et al., 2006). For an FWMC with a specific cross-sectional shape, the vortex structure in its wake is affected not only by the Reynolds number, as with a 2D cylinder, but also by its aspect ratio $AR = L/D$, where L represents the height of the cylinder and D represents the width of the cross-section, significantly. Sakamoto and Arie (1983) identified a "critical aspect ratio," AR_{cr}, below which 2D von Karman vortex street shedding is suppressed by downwash, and the time-averaged

Nomenclature

AR	Aspect Ratio	SSD	Scaled Spectral Density
AR_{cr}	critical aspect ratio	Δt	time step length
$b_i(z)$	initial coefficient at height of z	V	volume of the computational cell
C_D	drag coefficient	U_∞	inflow velocity
C_L	lift coefficient	$\bar{u}_i$, $\bar{u}_j$	filtered velocity
C_P	pressure coefficient	W	the total width of the computational domain
C_P'	fluctuating pressure coefficients	x	streamwise coordinates
D	width of the cross-section	y	normal direction coordinates
$E(z)$	total energy at height of z	y^+	non-dimensional cell distance from wall
$E_i(z)$	total energy of the ith mode at height of z	z	spanwise coordinates
$e(St,\zeta)$	modal energy density	Δ_f	filter-size
f	frequency	δ	thickness of the base-wall boundary layer
f_s	sampling frequency	δ_{ij}	Kronecker delta
H	height of the computational domain	ζ	dimensionless height
k_{sgs}	subgrid-scale kinetic energy	η_1	energy contribution to the overall flow field
L	height of the cylinder	η_2	energy contribution to the flow with a given frequency
$P(t_k)$	pressure at the kth moment	θ	direction angle
$\bar{p}$	filtered pressure	λ, λ_i	eigenvalue, eigenvalue of the ith mode
Q	second invariant of velocity magnitude	λ_2	second eigenvalues of the symmetric tensor
Re_D	Reynolds number based on D	ρ	density
S_{down}	distance from inlet to cylinder center	ρ_0	reference density
$\bar{S}_{ij}$	resolved strain rate tensor	$\Phi_i(z)$	the ith mode at height of z
S_{up}	distance from cylinder center to outlet	τ_{ij}	subgrid-scale stress tensor
St	Strouhal number	ν	kinematic viscosity
$St_{\sim}$	Strouhal number of certain modes as agreed in the text, e.g., St_1, St_2, St_3, St_{high}, St_{low} etc.		

wake structure changes from quadrupole to dipole (Sattari et al., 2012). The value of AR_{cr} ranges from 2.5 to 7, depending on the thickness of the base-wall boundary layer (δ) and the turbulence of the incoming flow (Kawamura et al., 1984; Luo, 1993; Hosseini et al., 2013).

When the aspect ratio exceeds the critical aspect ratio, the boundary layer and free-end downwash are unable to dominate the entire flow field, but instead reduce the flow velocity in the neighboring locations, leading to a decrease in the vortex shedding frequency. However, the frequency of vortex shedding will not vary continuously along the span. Vortex shedding manifests in distinct spanwise segments with diverse frequencies, leading to a cellular shedding vortex structure. Several vortices' cells with different Strouhal numbers ($St = fD/U_\infty$, where f is the shedding frequency, and U_∞ is the inflow velocity) are formed along the spanwise direction in the wake of the FWMC. This phenomenon is referred to as "cellular variation" (Lee, 1997; Kitagawa et al., 2002; Wang & Zhou, 2009; Moreau & Doolan, 2013), which results in multiple peaks in the far-field noise spectrum (Porteous et al., 2014). The number of cells increased with the aspect ratio. Cellular variation also occurs in the wake of circular cylinders in shear flow and can be described by the van der Pol oscillator (Griffin, 1985; Noack, 1991). Such an explanation can be applied to cells in the junction area (Porteous et al., 2014). Chen et al. (2022) demonstrated that a thick boundary layer ($\delta/D > 4$) inhibits the cellular variation of square FWMC at L/D = 6 or 10. For FWMC with a larger aspect ratio, prior research has overlooked the impact of a thicker boundary layer on wake structure. Consequently, the discussion on boundary layer thickness may be deemed negligible at this juncture.

In recent decades, comprehending flow characteristics facilitates the investigation of noise mechanisms of FWMCs. Porteous et al. (2017) conducted experiments to identify four shedding regimes of square FWMC relative to AR, namely R0 (L/D < 2), RI (2 < L/D < 10), RII (10 < L/D < 18), and RIII (L/D > 18). The number of noise peaks in these regimes is zero, one, two, and three, respectively. Yauwenas et al. (2019) conducted experimental and numerical measurements of the wake of square FWMCs with a range of 1.4 < L/D < 21.4, and identified the occurrence of cellular shedding when L/D >10. Demonstrating that cells are periodically shed in and out of phase with each other, resulting in the tonal nature of the noise emitted from FWMC. Similar acoustic phenomena were found in circular FWMC experiments (Moreau & Doolan, 2013). No tonal noise was observed when L/D < 9 (except at L/D = 3.2, where a weak peak noise appeared due to 3D vortex shedding, other than a vortex street). One dominant acoustic tone exists when 9 < L/D < 18, and two acoustic tones were found in the far-field when L/D > 18. By summarizing these results, it is evident that the flow and noise levels approach those of a 2D cylinder as the AR increases. Sound pressure levels generated by a square cylinder are 6–10 dB higher than those produced by a circular cylinder when the same aspect ratio and frontal dimension are considered. The AR has a greater influence on a circular cylinder compared to

square cylinders. Similar results are obtained by Becker et al. (2008) and King and Pfizenmaier (2009). The aforementioned studies address the distribution law of vortex shedding frequency with height and its correlation with far-field noise. However, there is a gap in the literature regarding the spanwise distribution law of vortex shedding amplitude.

Moreover, a low-frequency peak of circular FWMCs is usually explained by "tip-associated vortices" (Kitagawa et al., 1999), which were independent of the AR (Sumner et al. 2004) and midspan vortex shedding frequency. The St of this vortex is about 0.07 (Park & Lee, 2000, 2002, 2004). This vortex corresponds to the counter-rotating tip vortex of the "Krajnovic model" for circular FWMC wake (Pattenden et al., 2005; Frederich et al., 2008; Krajnovic, 2011). However, the previous literature did not directly link the noise at the tip area of the circular FWMC to the tip vortex in the Krajnovic model. In contrast, the flow and noise models of the square FWMC do not include any components related to the flow from the tip area. For example, in the "Bourgeois model" (Bourgeois et al., 2011, 2013; Hosseini et al., 2013), vortex filaments are periodically shed from either side of the square and are continuously linked at both extremities with connecting strands, forming a "full-loop" pattern in the near wake without tip vortex structure.

Various active or passive methods can be employed to reduce the aeolian noise generated by cylinders. The representative active control method to suppress vortex shedding and noise is suction on the windward side or blowing on the leeward side through holes or slots on the cylinder surface (Maryami et al., 2024; Maryami & Liu 2024). Vortex shedding is responsible for generating the noise around the cylinder as well as the trailing edge noise of the airfoil. Certain passive noise control strategies can reduce the noise by inhibiting vortex shedding, and techniques aimed at reducing trailing edge noise can also be employed to decrease noise generated by the cylinders. Porous materials are widely used in noise reduction of trailing edge (Bernicke et al., 2019; Ananthan et al., 2020). When applied to a cylinder, the best noise reduction effect is achieved by covering the free-end and along the span with porous material (Geyer, 2020). Filling porous materials in the grooves can also help reduce noise and drag (Moradi & Mojra, 2024). The splitter plate on the trailing edge of a circular cylinder can reduce noise by suppressing the large-scale vortex shedding behind the cylinder (Wang & Li, 2023), and a flexible splitter plate has a more significant effect (Duan & Wang, 2021). Biomimetic riblets create vortices and control the boundary layer, whose shape and orientation can influence the control effect of large-scale cavity structures behind the FWMC (Kadivar et al., 2024). A spanwise wavy-shaped cylinder wall causes the periodic vortex shedding to form bands instead of alternating oscillations, reducing flow fluctuations and far-field noise (Xiao & Tong, 2023; Qin et al., 2023). The dimples on the airfoil surface can reduce its trailing edge noise (Ananthan et al., 2022). Similarly, such structures on the cylindrical surface can also suppress vortex shedding, reducing drag and noise (Zheng et al., 2023). In addition, bio-inspired airfoil trailing edge noise control technology also has the potential to be applied to the cylinder (Bodling & Sharma, 2019; Ananthan & Akkermans, 2023). The above research demonstrates that the control means have different effects in different spanwise positions of FWMC; thus, it is necessary to clarify the distribution law of noise sources along the spanwise.

This study attempts to illustrate the noise contribution and pattern variation of each vortex shedding frequency in both tall square and circular FWMC noise spectra in the spanwise direction and propose a method for quantitatively determining the spanwise intensity distribution of each shedding frequency. To achieve these objectives, this study utilizes multiple spanwise transverse cross-sections for modal analysis instead of the longitudinal cross-sections commonly utilized in previous studies. Longitudinal cross-sections are less specific in displaying intensity distributions. As cellular variation is more noticeable near the free end, and there is currently no unified vortex shedding model for this phenomenon, this study focused on the upper part of the FWMCs. The aspect ratio here is set to be 13.6 (RII) to avoid discussion about the boundary layer. The distinction between the wakes of two types of FWMC near the free end has been highlighted, especially in relation to the flow pattern, intensity, and frequency of the tip-associated vortices of the circular FWMC. The far-field noise of long-span cylinders can be estimated utilizing the noise generated by a small span of the cylinder with a correction method (Kato et al., 1993; Seo & Moon, 2007). This study will discuss whether this method is suitable for FWMCs.

Here, large eddy simulation (LES) and Ffowcs Williams–Hawkings (FW–H) acoustics analogy results of square FWMC with AR = 13.6 is validated by comparing to experimental results from Moreau and Doolan (2013) in Section 2. These methods have been extensively utilized in this field (Afgan et al., 2007; Krajnovic, 2011; Saeedi & Wang, 2016; Lenz et al., 2019). Direct numerical simulation (DNS) and computational aeroacoustics are effectively utilized in simulating flow fluctuation and noise for 2D square and circular cylinders (Akkermans et al., 2015; Dawi & Akkermans, 2018). Strouhal number, pressure decay behavior, and lift and drag coefficients can all be obtained with good agreement with experimental results. Although DNS is computationally expensive for simulating 3D flows with high Reynolds numbers, it is still a potential alternative approach. The simulation results of the two FWMCs, including the time-averaged flow field, transient vortex patterns, pressure fluctuation spectrum along heights, and coherence with far-field noise, are compared in Section 3. In Section 4, DMD is applied to analyze the fluctuating pressure coefficient of several planes arranged in the spanwise direction of both FWMCs. Two types of energy contribution ratio parameters are introduced based on modal energy and plane location to analyze the distribution of spanwise shedding intensity. Finally, Section 5 summarizes the results and conclusions.

2. MODEL SETUP AND SIMULATION VALIDATION

Figure 1 is the sketch of the calculation models. The side width of the square cylinder and the diameter of the

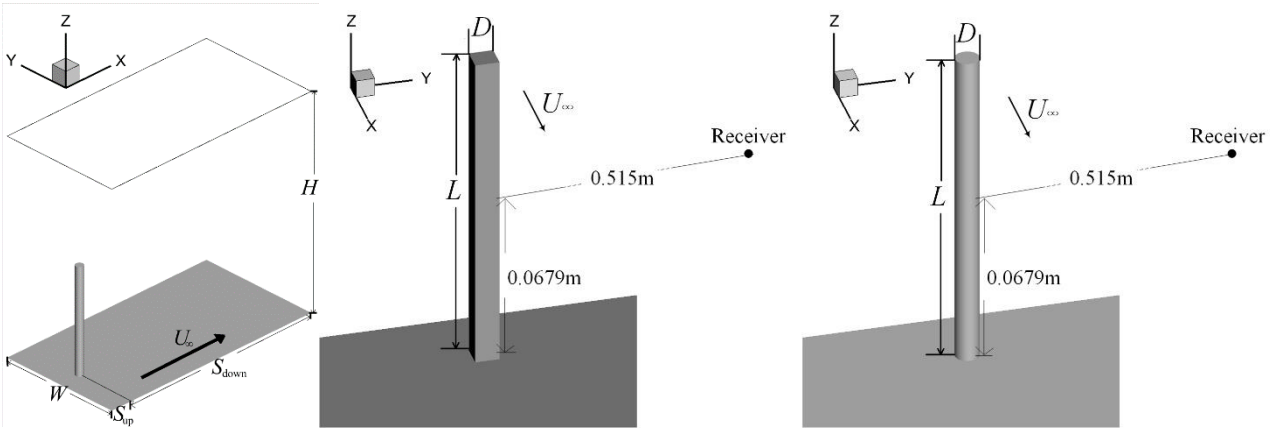

Fig. 1 Sketch of FWMC models and measure point location

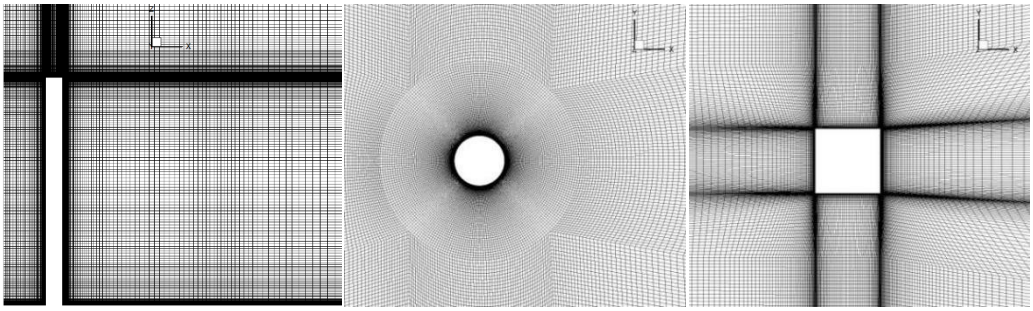

Fig. 2 Lateral (left, y = 0 plane) and vertical views (middle and right, z = 0 plane) of grid distribution around FWMCs

circular cylinder D = 0.01 m, and the height of the cylinders L = 0.136 m; thus, AR = 13.6. The origin of the coordinates is located in the center of the junction between the cylinder and the bottom surface. The x, y, and z coordinate axes correspond to the direction of incoming flow U_∞ (streamwise), the normal direction, and the direction of cylinder extension (spanwise), respectively. A velocity inlet boundary condition is set with U_∞ = 35 m/s and 0.33% turbulent intensity, located $S_{\text{up}} = 3D$ = 0.03 m upstream of the cylinder center. A zero-gauge pressure outlet boundary condition was applied $S_{\text{down}} = 27D$ = 0.27 m downstream from the cylinder center to ensure the full development of the wake. The total width of the computational domain $W = 16\,D$ = 0.16 m with the cylinder in the middle. The boundary condition of both sides is symmetry. The top of the grid is 0.139 m away from the free end of the cylinder, with symmetric boundary conditions. The total height of the computational domain $H = 27.5D$ = 0.275 m. The no-slip wall condition is applied to the bottom wall and the surfaces of the cylinders. The coordinate of the noise measure point is (0.0, 0.515, 0.0679) m. Reynolds number based on D $Re_D = 2.3 \times 10^4$.

ANSYS FLUENT 21.1.0 (2021) finite-volume solver is applied in the research. Because the Mach number of incoming flow is about 0.1, the simulation is assumed incompressible. The governing equation of incompressible LES is:

$$\frac{\partial \bar{u}_i}{\partial t} + \frac{\partial y}{\partial x_j}\left(\bar{u}_i \bar{u}_j\right) = -\frac{1}{\rho}\frac{\partial \bar{p}}{\partial x_i} + \nu \frac{\partial^2 \bar{u}_i}{\partial x_i \partial x_j} - \frac{\partial \tau_{ij}}{\partial x_j} \tag{1}$$

$$\frac{\partial \bar{u}_i}{\partial x_i} = 0 \tag{2}$$

where $\bar{u}_i$ represents the filtered velocity, $\bar{p}$ is the filtered pressure, ρ is the density, ν is the kinematic viscosity, and $\tau_{ij} = \overline{u_i u_j} - \bar{u}_i \bar{u}_j$ is the subgrid-scale stress tensor. The kinetic-energy transportation subgrid-scale model is employed, where τ_{ij} is modeled as:

$$\tau_{ij} - \frac{2}{3}\rho k_{sgs}\delta_{ij} = -2C_k \rho k_{sgs}^{\frac{1}{2}} \Delta_f \bar{S}_{ij} \tag{3}$$

where δ_{ij} is the Kronecker delta, $\bar{S}_{ij} = \frac{1}{2}\left(\frac{\partial \bar{u}_i}{\partial x_j} + \frac{\partial \bar{u}_j}{\partial x_i}\right)$ is the resolved strain rate tensor, $\Delta_f = V^{1/3}$ is the filter size, V is the volume of the computational cell, and $k_{sgs} = \frac{1}{2}\left(\overline{u_k^2} + \bar{u}_k^2\right)$ is the subgrid-scale kinetic energy. k_{sgs} is obtained by solving its transport equation, as referenced in Kim and Menon (1997). The values 1, 2, and 3 of i and j correspond to the incoming direction, horizontal direction, and spanwise direction, respectively. Pressure and velocity are coupled with the PISO algorithm. Spatial and temporal discretization schemes have second-order accuracy. Time step length Δt = 1×10^{-5}s. At first, 0.1 s physical time of simulation is conducted to get stable vortex shedding. Then, a 0.5 s physical time simulation is produced to obtain instantaneous data of the flow field and sampled with frequency of 10 kHz to compute far-field noise by FW–H equation. The source surface is located on the surface of the cylinders, and the FW–H formulation is solid. Structured grid is adopted. The height of the first layer of mesh is 6×10^{-6} m and $y^+ \approx 1$. Mesh distribution around the cylinders is illustrated in Fig. 2. From the side

Table 1 Aerodynamic coefficient results of square cylinder meshes with different cell numbers.

Cell number	$\overline{C_D}$	RMS C_D	RMS C_L
8.66×10^6	2.76	0.1553	0.9655
14.98×10^6	2.62	0.1319	0.8069
30.02×10^6	2.59	0.1348	0.8660

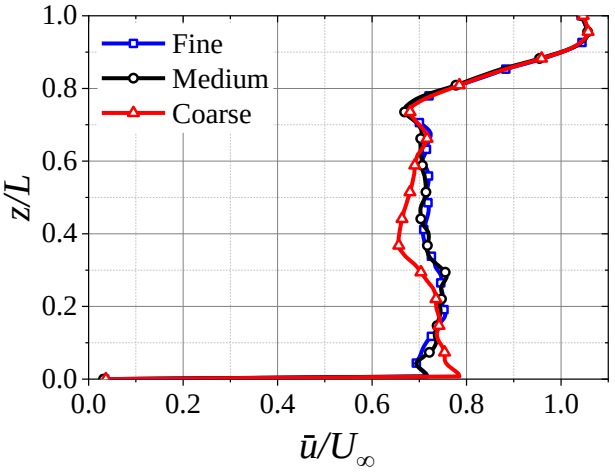

Fig. 3 Time-averaged spanwise profiles of u at x/D = 4 on plane y/D = 0.6

view (y = 0 plane), the grids of the two FWMCs are the same, and the grid around the cylinder under the overlooking view is the same as the grid on the bottom wall (z = 0 plane).

Three square cylinder meshes with approximately 9 million, 15 million, and 30 million cells are utilized to validate mesh independence. The number of grid points on each side of the square FWMC, span, and towards the side boundary of the computational domain is as follows: 50 × 120 × 84, 60 × 150 × 99, and 90 × 200 × 119. As discussed by Krajnovic (2011), improving cell number in this range may enhance simulation precision. However, it remains challenging to distinguish numerical errors from modeling errors.

Table 1 presents the aerodynamic coefficient results of the three meshes. Figure 3 presents the normalized spanwise time-averaged velocity distribution at the position x/D = 4 and y/D = 0.6 behind the cylinder. The results of medium mesh and fine mesh are quite close; thus, the medium mesh is chosen. The numerical result of the far-field noise spectrum from the medium mesh of the square FWMC is validated by comparing it to the experimental scaled spectral density (SSD) data presented by Moreau and Doolan (2013), as illustrated in Fig. 4.

The two tonal noise peaks of square FWMC are successfully obtained in the simulation. The amplitude simulation results are close to the experimental ones. A slight deviation exists in the main frequency simulation results. However, the simulation results for the main frequency still closely resemble the St of the 2D cylindrical flow, indicating that the numerical method has successfully captured the main flow phenomenon in the wake of FWMC. A 14-million mesh, approximating the

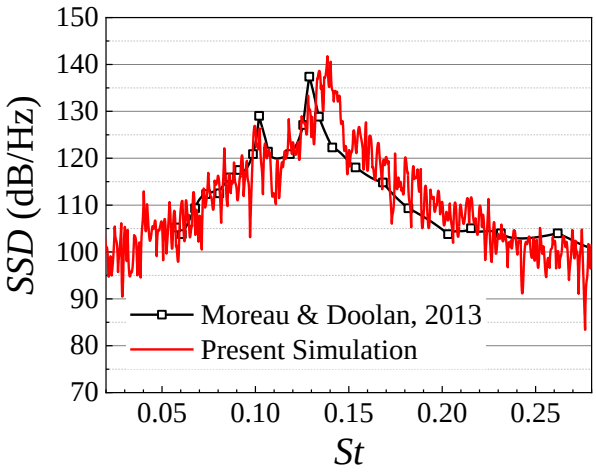

Fig. 4 Scaled power spectrum density validation of square FWMC at point (0.0, 0.0679, 0.515) m.

medium mesh for the square FWMC with 240 grid points on the circumference of the cylinder, is utilized for the simulation of the circular FWMC (see Fig. 2).

3. COMPARISON BETWEEN RESULTS OF SQUARE AND CIRCULAR FWMC

3.1 Wake Structure

This section compares the flow fields of the square and circular FWMC, providing a basis for subsequent analyses in Section 3.2. Figure 5 illustrates the time-averaged velocity and streamlines at different spanwise heights. A symmetric flow pattern similar to that of an infinite cylinder was observed. Near the top, the velocity behind the cylinder increases because of downwash. In the case of a circular FWMC, the wake vortex structure gradually moves toward the leeward side with the spanwise height increasing, without sudden morphological change.

Surface pressure coefficient (C_P) are presented in Fig. 6. The separation point remains stable along the spanwise direction, regardless of section shapes, indicating that cellular variation is not caused by the moving separation point. The pressure coefficient of the separation zone at the rear of the square FWMC increases with z/L decreasing, whereas the circular FWMC exhibits the opposite behavior. The minimum C_P peak located at $\theta \approx 135°$ varies between 1.5 and 2.2, which is lower than C_P = 5 observed in a 2D scenario and higher than C_P = 1 in cases of finite length with an aspect ratio of approximately 3.5 (Cao et al., 2019, 2022). λ_2 = -85,000 (Jeong & Hussain, 1995) iso-surface obtained with the time-averaged velocity gradient tensor, colored by the time-averaged streamwise velocity of the two FWMCs, is presented in Fig. 7. Three vortex zones can be observed in the FWMC wake, which are the vortices in the boundary layers of the bottom wall, vortices escaping from the cylinders in the middle and lower parts and vortices representing downwash emitted from the free end, known as braid vortices. And it aligns well with the results from Yauwenas et al. (2019).

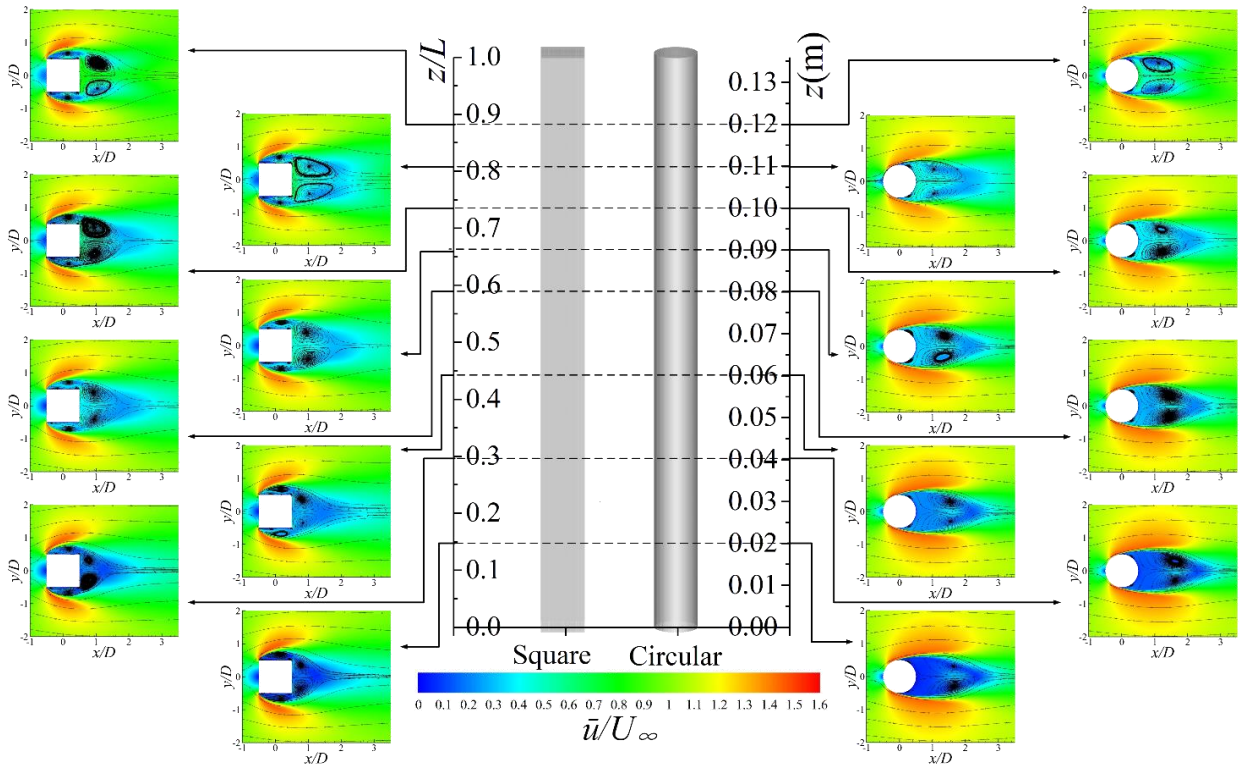

Fig. 5 Time-averaged dimensionless velocity magnitude $\bar{u}/U_\infty$ distribution and streamlines in several planes of square and circular FWMC wakes.

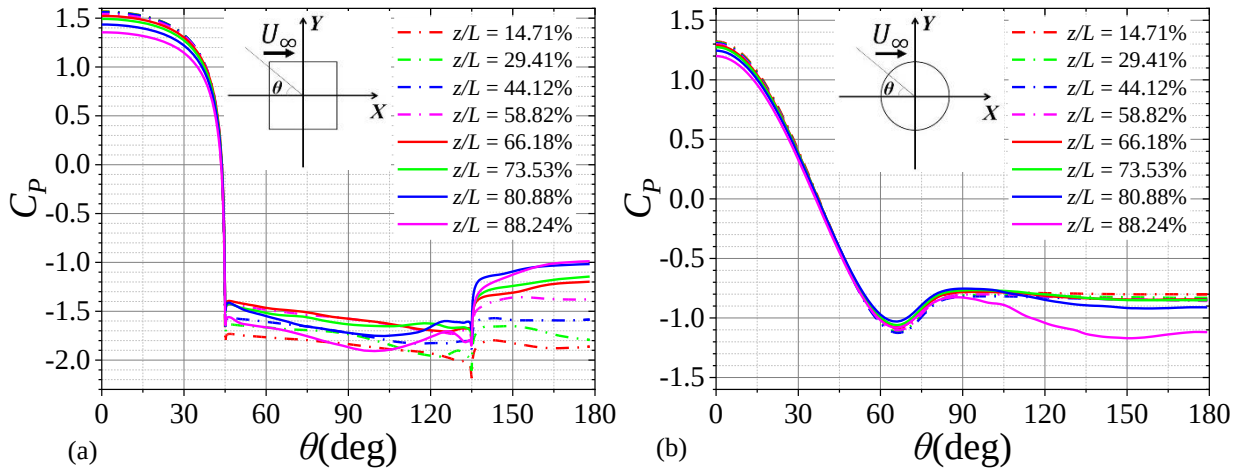

Fig. 6 Surface pressure coefficient in different planes of square (a) and circular (b) FWMC

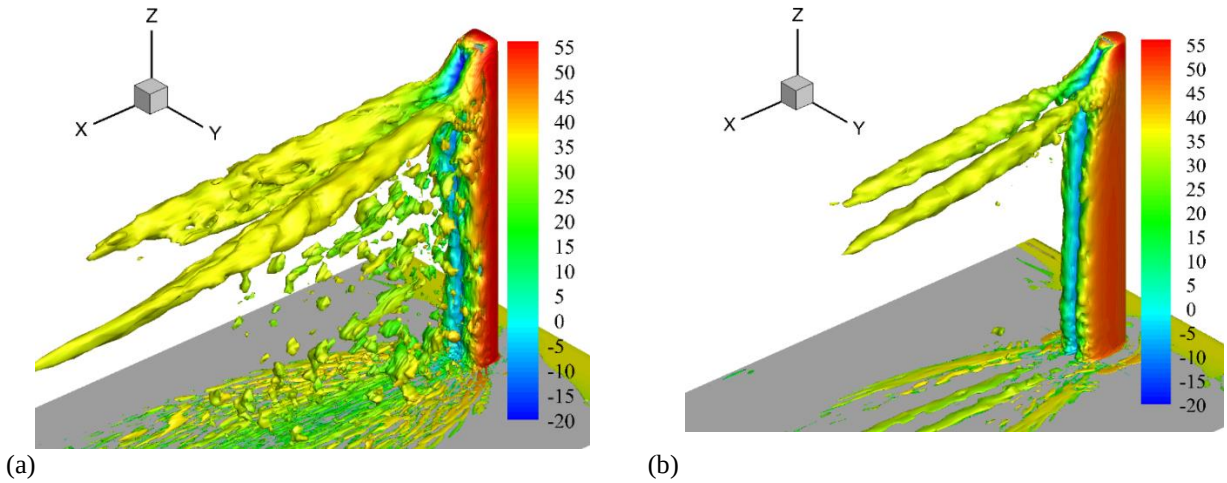

Fig. 7 λ_2 = -85,000 iso-surface colored by time-averaged streamwise velocity (m/s) of square (a) and circular (b) FWMC wakes

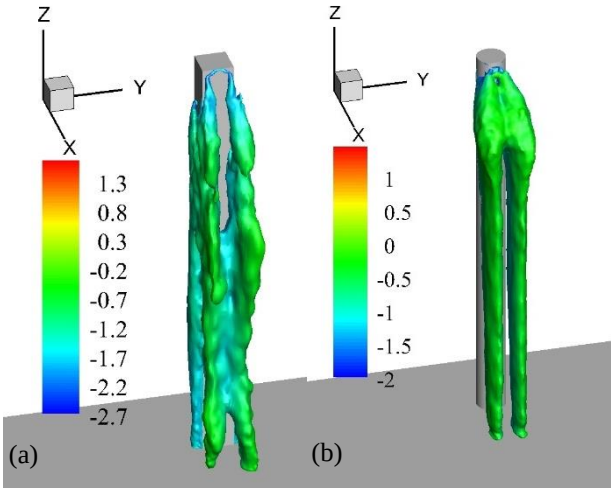

Fig. 8 Iso-surface of pressure coefficient mean square root colored by mean relative pressure coefficient, 0.7 for square (a) and 0.4 for circular (b)

By comparing the two cylinders, the square FWMC has more intense vortices that continue downstream in the lower and middle span, while the circular FWMC has the lower and middle vortices gathering around the cylinder. At the wall end, the circular FWMC exhibits more continuous vortices, whereas the square FWMC displays more fragmented vortices.

Figure 8 presents an iso-surface of RMS C_P = 0.7 in the square FWMC wake and RMS C_P = 0.4 iso-surface in the circular FWMC wake colored with the mean relative pressure coefficient. A quite different pressure fluctuation spanwise distribution is observed between square and circular FWMCs, which corresponds well to Fig. 5.

Q = 1 × 10^7 iso-surfaces colored by vorticity magnitude are presented in Fig. 9 to illustrate the general shape of the instantaneous flow field. The instantaneous flow field is highly unsteady and asymmetric. The vortex shedding at different heights does not form a 3D vortex system connecting the entire span of the cylinder but rather a series of cells, especially in the upper part. The phase and frequency of the shedding vortex vary according to the heights. It indicates that the Bourgeois model is not applicable under the given AR and Re conditions. In Fig. 7, both FWMCs exhibit braid vortices at the tip, but this structure is not evident in the instantaneous result presented in Fig. 9.

In terms of fluid field, the pressure fluctuation spanwise distribution between square and circular FWMCs are quantitively different. How this pressure fluctuation spanwise distribution impacts the far-field noise spectrum will be discussed in Section 3.2. The above results include no significant segmentation of the flow field in the spanwise direction. The reason for cellular variation could not be found in instantaneous or time-averaged flow field results.

3.2 Coherence Between Spanwise Velocity Fluctuations and Far-Field Noise Spectrum

The normalized scaled spectral densities of far-field noise from both FWMCs at measurement points are presented in Fig. 10. There are two tonal noise peaks at St = 0.1 and 0.14, respectively, in the spectrum of square FWMC, the tonal noise with $St \approx 0.14$ has a larger

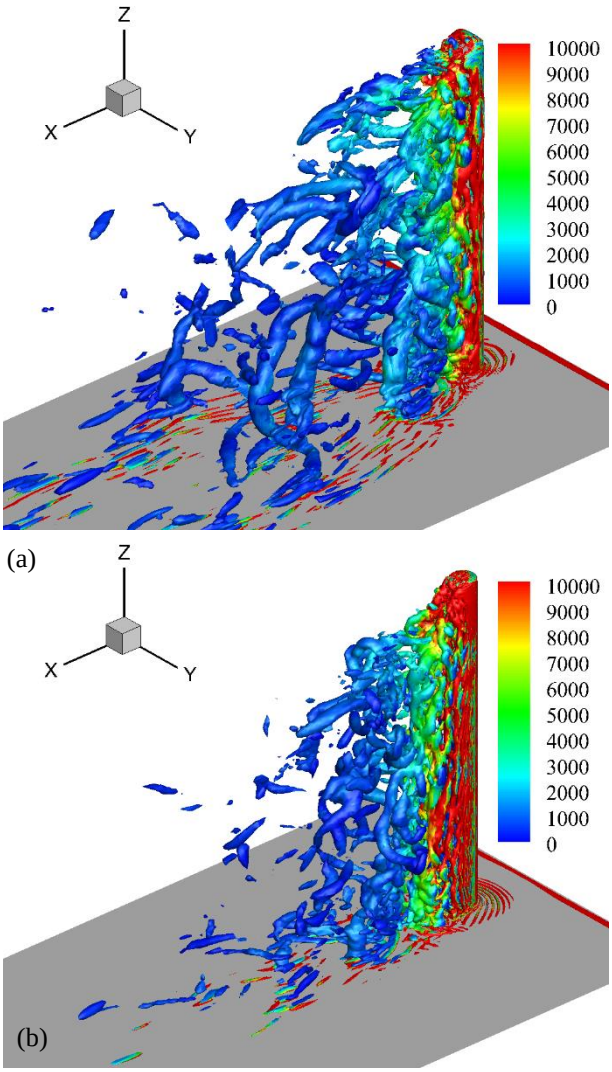

Fig. 9 Q = 1 × 10^7 iso-surface of instantaneous field colored by vorticity magnitude (s^{-1}) of square (a) and circular (b) in FWMC wakes

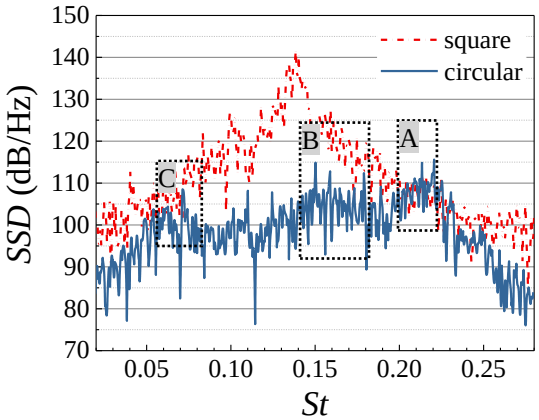

Fig. 10 Scaled power spectrum density at measure point (0.0, 0.0679, 0.515) of square and circular FWMC

amplitude, which is associated with a 2D Von Karman vortex street (Porteous et al., 2017). The St = 0.1 peak is close to the vortex shedding frequency of a short-span (AR = 4) square FWMC (Sattari et al., 2012; Bourgeois et al., 2013; and Saeedi & Wang, 2016). For the circular FWMC, the St band with the maximum amplitude is around 0.22 (marked by A in Fig. 10) which corresponds to the 2D vortex shedding frequency. Other St bands with relatively high amplitude values are approximately 0.07 and 0.15 to 0.19 (marked by C and B, respectively).

Figure 11(a) illustrates the spectra of fluctuating velocity at x = 0.02 m and y = 0.005 m along spanwise of the square cylinder, which matches well with the experimental results of Moreau and Doolan (2013). The distribution of velocity fluctuations can be observed as follows: when z/L < 0.6, St of fluctuating velocity is about 0.14, for z/L between 0.5 and 0.9, $St \approx 0.1$, and z/L > 0.9, the fluctuation disappears because of the downwash flow above the free end. Figure 11(b) illustrates the relationship between the near-field flow pattern and far-field noise, which is established by calculating the coherence of velocity fluctuation in the time domain and far-field sound pressure in the frequency domain, considering the sound propagation time delay. The results are filtered to highlight the parts with coherence > 0.7 (the filtered equation $f(x) = \frac{1}{2}\tanh(5(x-0.7)+1)$). In the range of z/L < 0.6, the highest coherence occurs at $St \approx$ 0.14. When z/L > 0.6, the highest coherence occurs at St ≈ 0.1. The causality between the flow phenomena around the lower part and the main noise peak at $St \approx 0.14$ has been demonstrated. While the tonal noise at $St \approx 0.1$ is associated with flow fluctuations in the upper part (z/L > 0.6).

The same analysis method is applied to a circular cylinder. The fluctuating velocity and filtered coherence of a series of points at x = 0.02 m and y = 0.005 m in the flow field around a circular cylinder along the Z axis are presented in Fig. 12(a) and (b). Regarding the circular FWMC, Fig. 12(a) demonstrates that the spectra of fluctuating velocity reach their maximum value when z/L < 0.6 and exhibit a far-field tonal noise at $St \approx 0.22$. Figure 12(b) describes three areas of high coherence at different spanwise positions, and three groups of corresponding relationships between the z/L ranges and St can be identified by comparing Figs. 10 and 12(b). That is, A) z/L < 0.6 and $St \approx 0.22$, B) 0.5 < z/L < 0.9 and 0.15 < St < 0.19, and C) 0.85 < z/L < 0.95 and $St \approx 0.07$. The areas in both figures are also denoted by A, B, and C. The simulation findings agree with the experimental results of Moreau and Doolan (2013) in terms of the St and spanwise range.

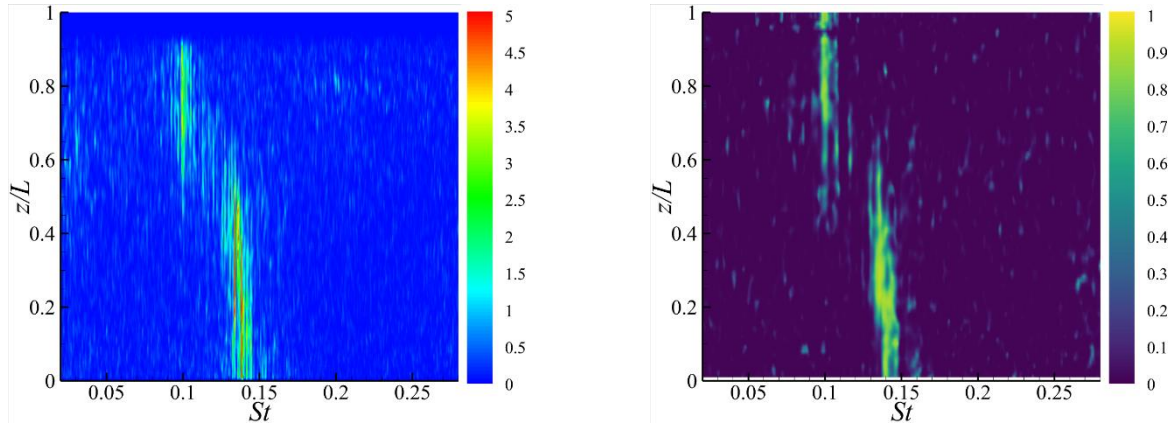

(a) Fluctuating Velocity Spectra (m/s) (b) filtered Coherence

Fig. 11 Spanwise distribution of fluctuating velocity and its coherence with far-field noise spectrum at x/D = 2, y/D = 0.5 of flow field of finite square cylinder

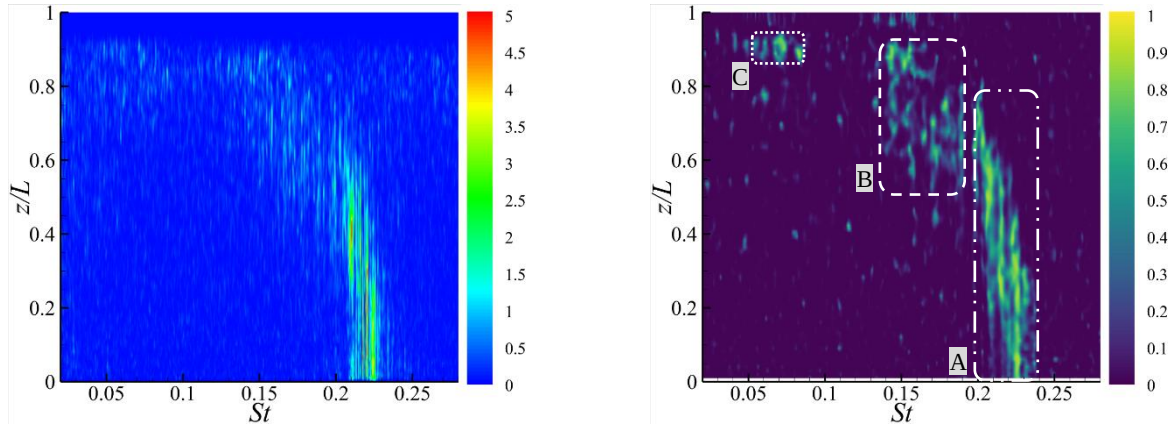

(a) Fluctuating Velocity Spectra (m/s) (b) filtered Coherence

Fig. 12 Spanwise distribution of fluctuating velocity and its coherence with far-field noise spectrum at x/D = 2, y/D = 0.5 of flow field of finite circular cylinder

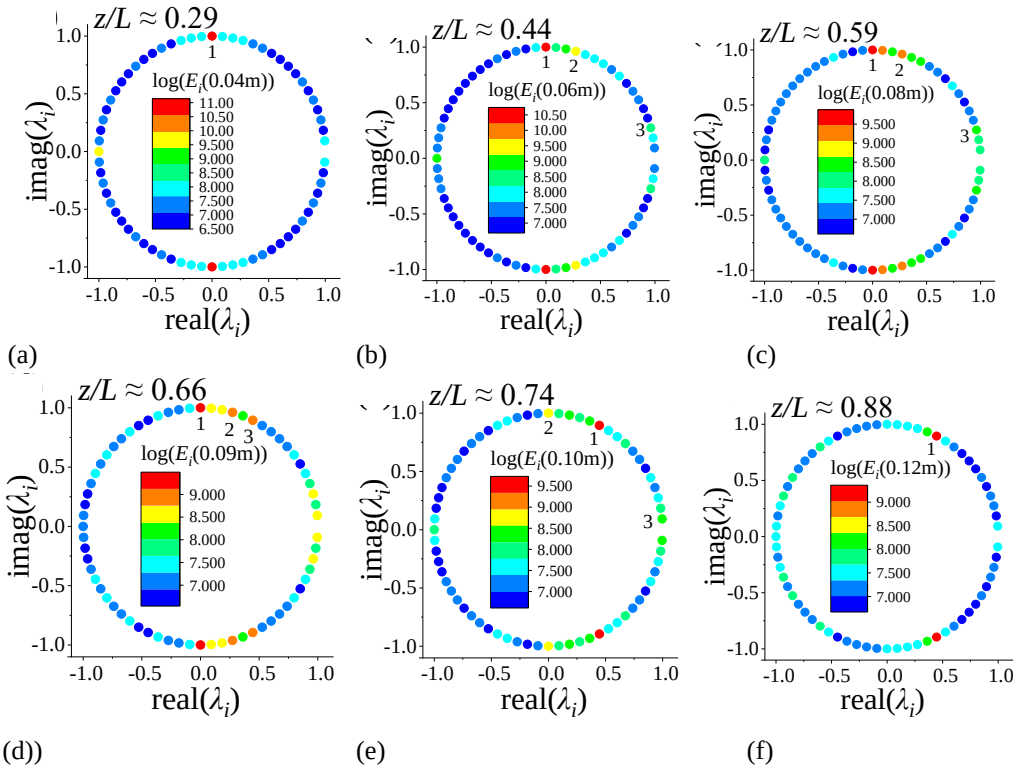

Fig. 13 Distribution of eigenvalues of DMD modes of square FWMC wakes at each height on complex plane

By comparing Figs. 11 and 12, it is concluded that in the upper part (z/L > 0.6), there is only one fixed frequency value in the far noise field of the square FWMC. In contrast, there are multiple noise frequencies near the free end for the circular cylinder. Flow phenomena with a specific frequency and height distribution range can be identified as the source of far-field noise.

In summary, cellular variation is a phenomenon that only occurs in the frequency domain and is not directly reflected in the flow field. Only one cellular variation occurred in the middle and upper part of the square FWMC, and the tip vortex system did not affect the vortex shedding frequency. The circular FWMC exhibited cellular variation several times along the midspan and the tip area.

4. MODAL ENERGY SPANWISE DISTRIBUTION ANALYSIS UTILIZING DMD

4.1 Conventions

In this section, 68 snapshots of fluctuating pressure coefficients C_P' are captured in the two FWMC flow fields, and DMD modes are calculated in several sections along the spanwise, where:

$$C_P'(t_k) = \frac{P(t_k) - \overline{P}}{\frac{1}{2}\rho_0 U_\infty^2}, k = 1, 2, \dots, n \tag{4}$$

Here, ρ_0 = 1.225kg/m^3, $\overline{P} = \frac{1}{n}\sum_{k=1}^{n} P(t_k)$, n = 68, $P(t_k)$ represents the pressure at the kth moment. Sampling frequency f_s = 2000 Hz and mode frequencies are nondimensionalized as $St = fD/U_\infty$. Flow phenomenon with St < 0.29 (or $f \le$ 1000 Hz = 0.5f_s) can be obtained. The time-averaged value was subtracted from the data results in the DMD mode with a frequency of 0, which represents the time-averaged field (eigenvalue λ = 1) and has an amplitude of 0. Therefore, the noise source is better characterized. The total energy of the ith mode at the height of z is denoted as $E_i(z)$, and the total energy of this section, denoted $E(z)$, can be expressed as:

$$E_i(z) = \sum_{j=1}^{n} \left\| \lambda_i^{j-1} b_i(z) \Phi_i(z) \right\|_F^2 \tag{5}$$

$$E(z) = \sum_{i=1}^{n} E_i(z) \tag{6}$$

Here, λ_i is the corresponding eigenvalue, $b_i(z)$ is the initial coefficient at a height of z and $\lambda_i^{j-1} b_i(z)$ is the time coefficient of the ith mode $\Phi_i(z)$ of this location at the jth moment.

4.2 Selection and Description of Major Modes

Figures 13 and 14 depict the real and imaginary parts of the eigenvalues for each mode of each plane in the square and circular FWMC wake. The eigenvalues of DMD modes at a specific height are predominantly distributed around the unit circle in the complex plane, indicating that these modes remain stable over time. Furthermore, the St distribution of eigenvalues remains consistent across all heights in these figures. Specifically, the eigenvalues of all modes at different heights fall within -33–34 times the $\Delta St \approx 0.0084$. Therefore, connections can be established between flows of the same frequency at different altitudes. Positive frequency modes are chosen to represent the conjugate pair. The mode with λ = -1 is ignored. Modes that meet the following conditions are

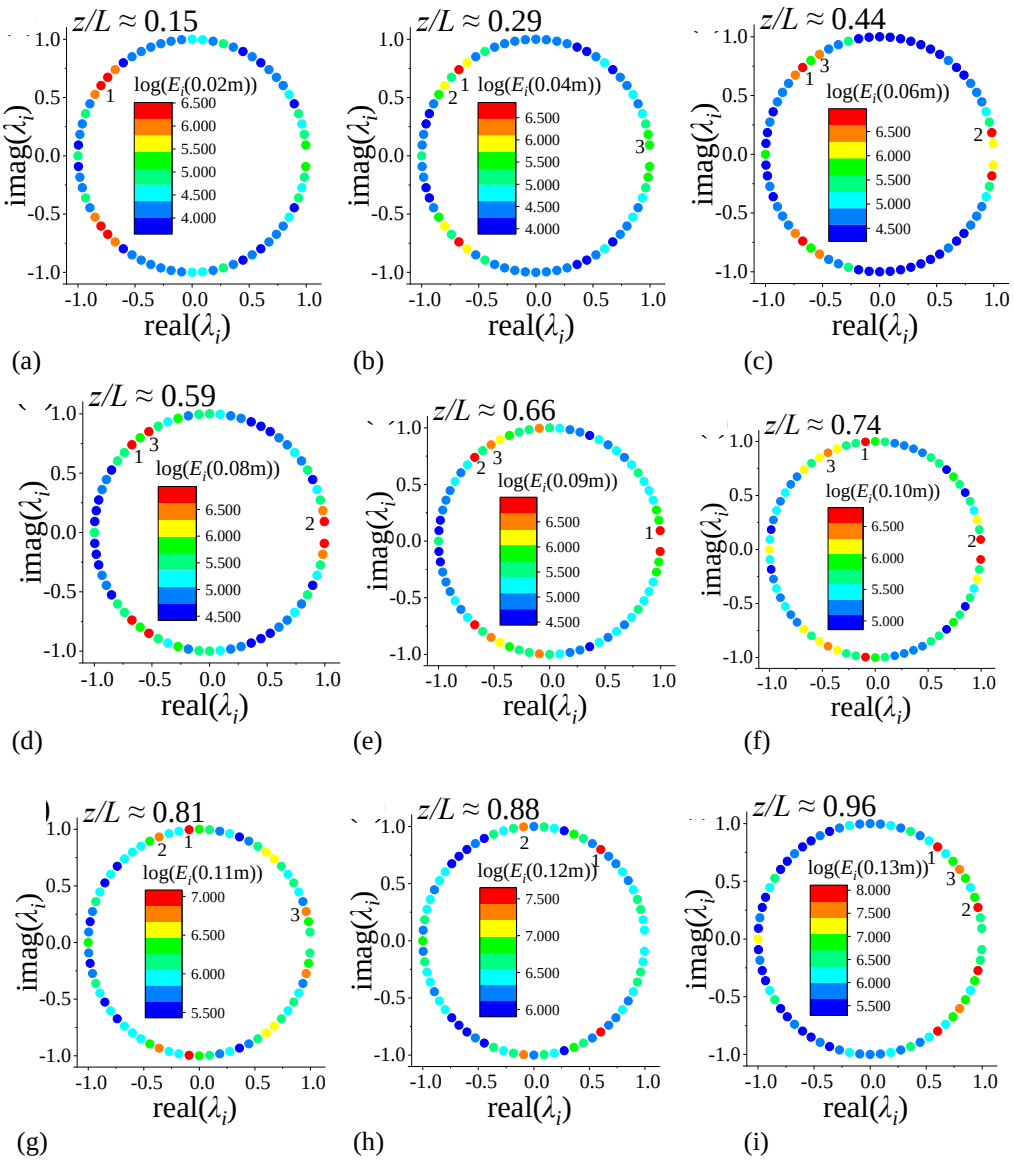

Fig. 14 Distribution of eigenvalues of DMD modes of circular FWMC wakes at each height on complex plane

marked on the graph: first, $E_i(z)$ is a local maximum value; second, $E_i(z)/E(z) > 2.5\%$; third, they satisfy the former two conditions and have the top three $E_i(z)$ values. These modes will be assigned the codes of Modes 1, 2, and 3 according to the value of $E_i(z)$ in descending order, and their Strouhal numbers are noted as St_1, St_2, and St_3. If fewer than three modes meet these conditions, only one or two modes will be listed.

Figures 15 and 16 present the real components of these three major modes. In the case of the square FWMC (Fig. 15), the first three high-energy modes in each height might correspond to the different frequencies. The high-frequency modes are $St_{high} \approx 0.10$, 0.12, and 0.14, which all demonstrate antisymmetric patterns and correspond to the morphology of the von Karman vortex street. The low-frequency mode is $St_{low} \approx 0.02$, which are symmetric. Symmetric mode occurs when two high-frequency modes simultaneously appear, and $St_{low} = St_{high1} - St_{high2}$, for instance $St_{low} \approx 0.02 = 0.14 - 0.12$, as illustrated in Fig. 15(b). When two signals of similar frequency and amplitude are superimposed, they will periodically reinforce and cancel each other out. This results in the low-frequency components appearing in the spectrum. This phenomenon corresponds to the periodic change in amplitude, which was named "nonlinear beat" by earlier researchers and has been observed in experiments and numerical research (Noack, 1991).

In addition, the mode with $St_{high} = 0.12$ only appears within a limited range of span ($0.44 < z/L < 0.66$) resulting in a small amount of energy in total; hence, their influence on the far-field noise can be ignored.

No mode corresponding to the braid vortices in the time-averaged flow field near the tip of the square FWMC was identified. By comparing images of flow patterns at various heights in the upper part of the FWMC, as illustrated in Fig. 15, it is observed that the vortex behind the cylinder is compressed because of downwash flow from the free end.

For the circular FWMC (Fig. 16), modes with $St \geq 0.08$ exhibit the typical antisymmetric pattern of a von Karman vortex street. In addition to the plane near the top, the low-frequency modes ($St < 0.05$) are symmetric. In the midspan ($0.44 < z/L < 0.88$), symmetric modes exhibit

nonlinear beat at this height. In the highest plane, $z/L \approx 0.96$ (z = 0.13 m), three main modes have been identified. Mode 1, with $St_1 \approx 0.08$, has been previously discussed. Mode 2, with $St_2 \approx 0.03$, differs from the previous low-frequency modes and may be related to nonlinear beat phenomena. Mode 3 is symmetric and satisfies $St_3 = St_1 - St_2 \approx 0.06$, demonstrating "tip-associated vortices" (Moreau & Doolan, 2013). The analysis above indicates that both noise bands A and B in Figs. 10 and 12(b) are produced by von Karman vortex streets influenced by cellular variation. In contrast, Band C is formed by both antisymmetric flow from the cylinder surface and symmetric flow from the top. No tonal noise corresponds to the tip-associated vortices in the spectrum of the square FWMC, while braid vortices are present in its time-averaged flow field. Therefore, the tip-associated vortices are considered to be different from the braid vortices in the time-averaged flow field, as illustrated in Fig. 7.

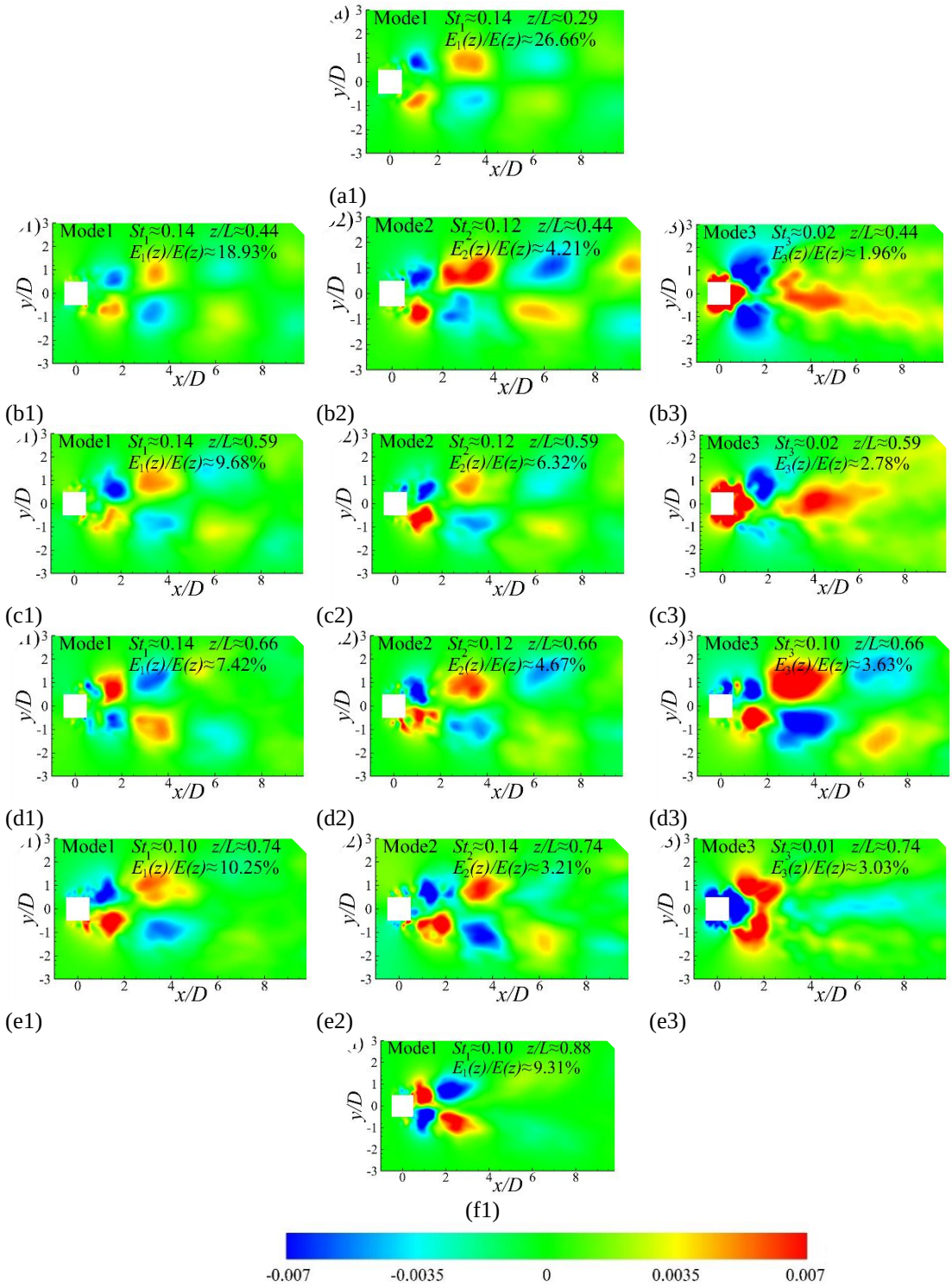

Fig. 15 Real parts of major DMD modes of square FWMC wakes: (a) z = 0.04 m; (b) z = 0.06 m; (c) z = 0.08 m; (d) z = 0.09 m; (e) z = 0.10 m; (f) z = 0.12 m

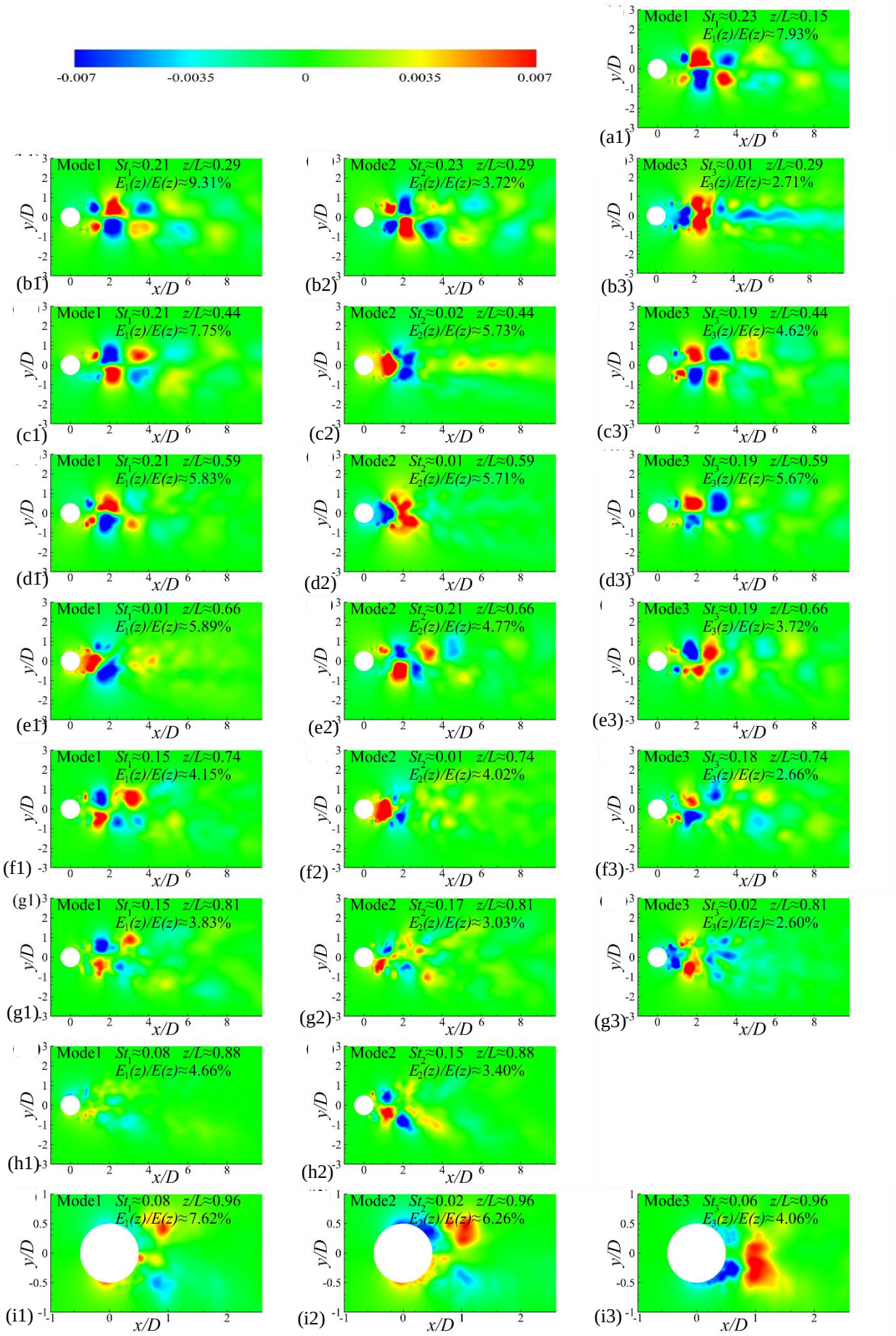

Fig. 16 Real parts of major DMD modes of circular FWMC wakes: (a) z = 0.02 m; (b) z = 0.04 m; (c) z = 0.06 m; (d) z = 0.08 m; (e) z = 0.09 m; (f) z = 0.10 m; (g) z = 0.11 m; (h) z = 0.12 m; (i) z = 0.13 m

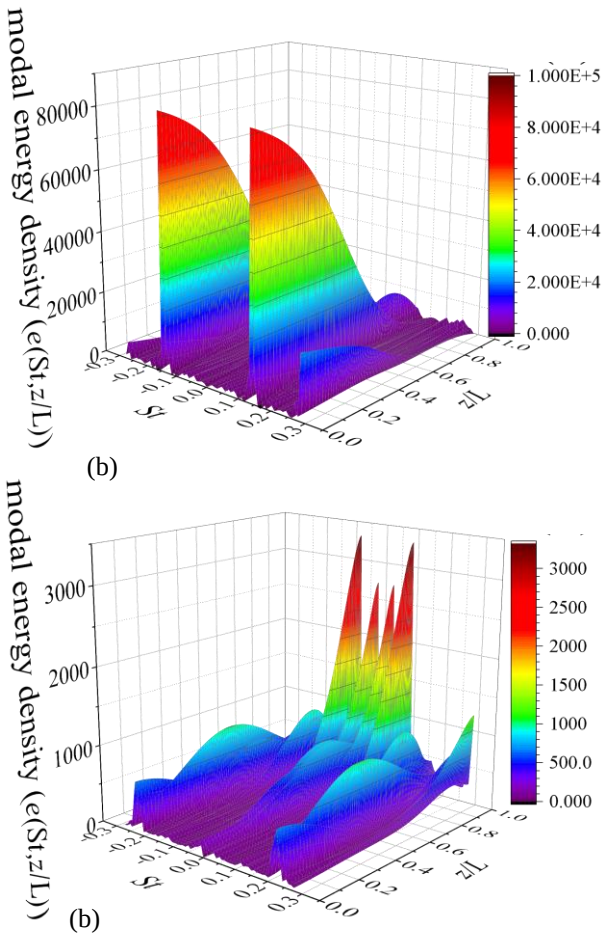

Fig. 17 Modal energy density $e(St,\zeta)$ of square FWMC (a) and circular FWMC (b)

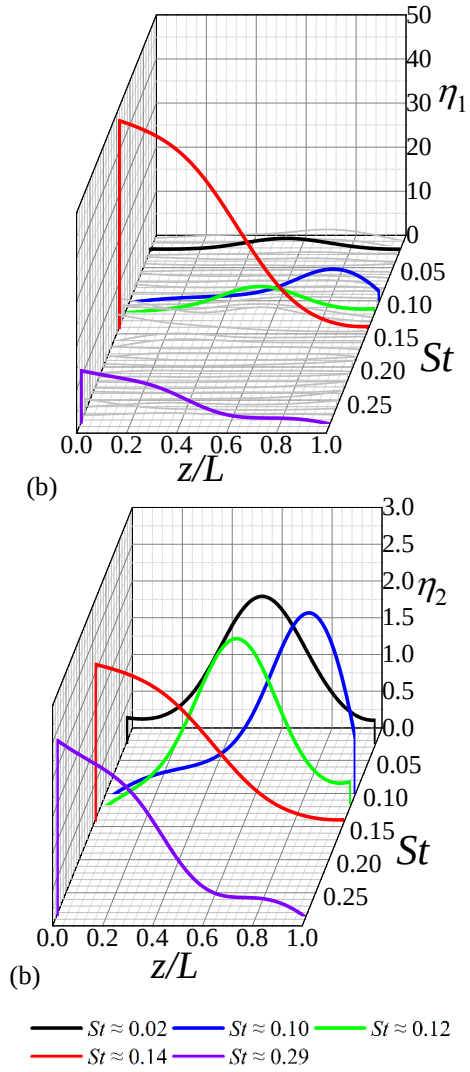

Fig. 18 Waterfall diagram of overall energy contribution density, η_1 (a) and energy contribution density to particular St, η_2 (b) of square FWMC

4.3 Spanwise Distribution of Model Energy Density

St is considered an independent variable for investigating the distribution of energy. As illustrated in Fig. 17, the modal energy density at a specific St and dimensionless height $\zeta = z/L$ is obtained from DMD operation and expressed as $e(St,\zeta)$, which satisfies:

$$\int_{-33\Delta St}^{34\Delta St} e(St,\zeta)dSt\Big|_{\zeta=z/L} \approx E(\zeta) \tag{7}$$

where ΔSt is the step of St in DMD, and there are 68 modes utilized in total, with St varying from -33ΔSt to 34ΔSt.

This article defined two types of energy contribution parameters to estimate the energy distribution along the spanwise direction, as expressed in Eqs. (8) and (9).

$$\eta_1(St,\zeta) = \frac{e(St,\zeta)}{\int_{-33\Delta St}^{34\Delta St}\int_0^1 e(St,\zeta)d\zeta dSt} \tag{8}$$

$$\eta_2(St,\zeta)|_{St=St_i} = \frac{e(St,\zeta)}{\int_0^1 e(St,\zeta)d\zeta\Big|_{St=St_i}} \tag{9}$$

Where η_1 represents the energy contribution to the overall flow field and η_2 refers to the energy contribution to the flow with a given frequency St_i. It is easy to obtain Eqs. (10) and (11).

$$\int_{-33\Delta St}^{34\Delta St}\int_0^1 \eta_1(St,\zeta)d\zeta dSt = 1 \tag{10}$$

$$\int_0^1 \eta_2(St,\zeta)d\zeta\Big|_{St=St_i} = 1 \tag{11}$$

This implies that the integral of η_1 over St and ζ signifies the percentage of the modal energy contribution of the unsteady flow within a specific range to the overall flow field, whereas the integral of η_2 over ζ signifies the percentage of the flow with the frequency of St_i in the span range to the total energy at this frequency.

For square FWMC, the results of η_1 and η_2 with positive St are presented in waterfall diagrams (Fig. 18). Dominant frequencies are highlighted in colors, and the minor modes are in grey in Fig. 18(a) and omitted in Fig. 18(b). First, the flow with $St \approx 0.14$ contains the majority of the energy in the overall flow field. It and its conjugate modes contribute 37% of the overall modal energy. Different from that of infinite 2D square wake flow, about 60% of the modal energy of $St \approx 0.14$ mode is concentrated in the middle-low part, which is below z/L

= 0.3 because of the 3D impact. A similar phenomenon is observed for $St \approx 0.29$, which is double the frequency of $St \approx 0.14$. Second, more than 60% of the energy of $St \approx 0.10$ is concentrated above $z/L = 0.7$, which is caused by the down-washing flow. The conjugate modes of this frequency contribute 5% to the overall modal energy. The flow of $St \approx 0.14$ and $St \approx 0.10$ is the main source of far-field noise. The transition mode, characterized by $St \approx 0.12$, has 4% overall contribution and over 70% of its energy concentrated in the range of z/L from 0.3 to 0.7. This frequency makes a minimal contribution to the modal energy of the overall wake without a corresponding far-field noise spectrum peak. A similar situation for the nonlinear beat flow with $St \approx 0.03$ contains 3% overall modal energy contribution with its conjugate mode and over 65% of its energy distributed in the span range of 0.3 L–0.7 L. The contribution of other St flows to the overall flow field can be ignored.

For circular FWMC, the results of η_1 and η_2 with positive St are summarized in Fig. 19. For Strouhal numbers in the noise band A (as presented in Fig. 12), the modal distribution energy of $St \approx 0.21$, corresponding to the 2D infinite circular cylinder vortex shedding frequency, is mainly concentrated in the middle part with z/L range of 0.3–0.7. And 55% energy of $St \approx 0.23$ is distributed below z/L = 0.4. The modal energy contribution ratio of the two frequencies to the overall flow field is 7% and 3%, respectively. For Band B, the value of St decreases from 0.19 to 0.15, causing more than 50% of the energy to shift from z/L = 0.4 to z/L= 0.95. The smaller the value of St, the greater the concentration of energy in the upper part. The overall modal energy contribution ratio of each frequency is approximately 3%. In Band C, the energy is predominantly concentrated near the upper region. Over 70% of the energy flux with $St \approx 0.08$ is concentrated at z/L = 0.8, as well as $St \approx 0.02$. The overall modal energy contribution of both frequencies is approximately 6%. Though the flow distribution range at the top is relatively narrow, it possesses significant energy and results in noticeable noise in the far-field. The frequency Bands A and B can be considered a result of gradual cellular variation across almost the entire span of the circular FWMC, excluding the tip area. The noise in frequency Band C is caused by tip-associated vortices. Compared with the modal energy of square FWMC, which is concentrated in a single frequency ($St \approx 0.14$), the circular FWMC energy is more dispersed, with relatively large modal energy contribution frequencies at $St \approx 0.02$, 0.08, and 0.21.

Combining the results of square and circular FWMC from Figs. 18 and 19, it can be found that the energy contribution for the circular FWMC is greater in the upper portion and smaller in the lower portion. In contrast, the modal energy of the square FWMC mainly concentrates in the lower part. This corresponds to the pressure mean square root distribution rule depicted in Fig. 8. And it indicates that, for both circular and square FWMC, the correlation between the flow fluctuation and the far-field noise spectrum characteristics varies along the spanwise of the FWMC. Furthermore, the assumption of "statistical

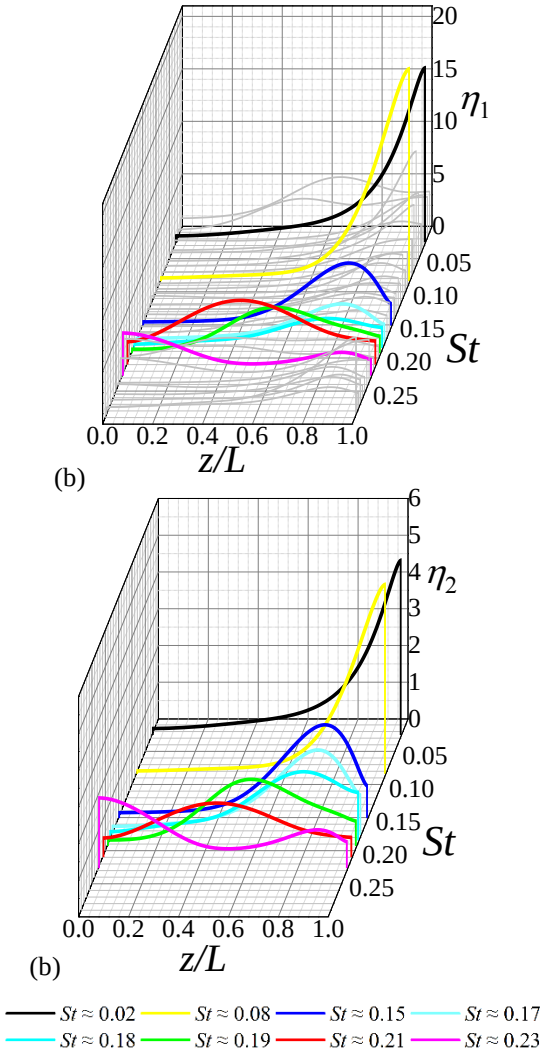

Fig. 19 Waterfall diagram of overall energy contribution density, η_1 (a) and energy contribution density to particular St, η_2 (b) circular FWMC

homogeneity in the spanwise direction" is not satisfied in this situation. Therefore, applying the correction method from Kato et al. (1993) or Seo and Moon (2007) to estimate far-field noise applied to FWMCs near free-ends or junction areas could be further discussed or modified.

The shedding frequency of 2D von Karman vortices depends on the fluid's viscosity (usually constant), the size of the blunt body, and the incoming flow velocity. For a 3D cylinder, if the distribution of the width (which determines the intensity of the shedding vortices) and the velocity of the incoming flow is known, the cellular distribution of the vortex shedding frequency can be determined (Noack, 1991). The decrease in vortex shedding frequency near the free end of the FWMC can be explained by the downwash flow at the free end reducing the local incoming flow velocity or changing the direction of local flow. Combined with the distribution of the modal energy of the two FWMCs and the sound source structure analysis, the circular cylinder's low-frequency tip-associated vortices strengthen the pressure fluctuations in this area. This requires the lower and middle 2D vortex shedding frequencies ($St \approx 0.21$) to pass

through more frequencies to transition to the lower frequency ($St \approx 0.08$) in the upper part. While the square FWMC has no structure corresponding to the noise at the free end, the vortex shedding frequency of the upper part is not significantly different from that of the middle and lower parts, resulting in a small number of vortices shedding frequency cells generated. And more modal energy is also distributed in the middle and lower parts of the cylinder. In further research, if several physical quantities can be extracted from the flow field with distributions similar to the modal energy along the spanwise direction revealed here, it is possible to directly estimate the cellular variation of FWMC from these quantities. The computational cost of estimating cellular vortex shedding from FWMC and its vibration and far-field noise may be significantly reduced.

5. CONCLUSION

A hybrid acoustic method of LES combined with FW–H equation is utilized to investigate the flow field and far-field noise around FWMCs with square and circular cross-sections. The AR of both FWMCs is 13.6. Numerical results comparing square and circular FWMCs are analyzed from various perspectives. DMD is performed to deal with the fluctuating pressure coefficients at different heights of the FWMCs. Two types of modal energy contribution ratios are introduced to quantitively describe the spanwise distribution of flow phenomena. In summary, the following conclusion can be drawn.

- For the square FWMC, the main far-field noise peak at $St \approx 0.14$ comes from the height span below 0.3 L. The secondary noise peak with $St \approx 0.10$ was generated from the height span above 0.7 L. In the midspan (0.3 L –0.7 L), where modes of both frequencies exist simultaneously, a transition mode of $St \approx 0.12$ is identified without significant noise contribution to the far-field noise spectrum.
- For the circular FWMC, two vortices cells correspond to the main noise band ($0.2 < St < 0.23$) of circular FWMC distributed below 0.7 L. During this span, the cell frequencies are relatively concentrated. The vortices cells in the noise band of $0.15 < St < 0.19$ distributed from the midspan to the upper part in a dispersed manner. The noise band with $St \approx 0.08$ corresponds to tip-associated vortices gathering in the span above 0.8 L.
- For any height of both cylinders, if there are two primary modes simultaneously, a symmetrical low-frequency nonlinear beat mode will occur with a frequency equal to the frequency difference of these two modes. This low-frequency mode does not exhibit a response in the far-field noise spectra.
- The modal energy of circular FWMC is more concentrated near the top, while that of square FWMC is concentrated at the lower part. The far-field sound pressure level of FWMCs cannot be estimated via the correction method that assumes the amplitude of acoustic pressure radiated from each subsection of the cylinder is the same.

The conclusions mentioned above are contingent upon the cross-sectional shape of the square and circle, the prevailing aspect ratio within the range of RII (10–18), and the incoming flow conditions of the subcritical Reynolds number. However, the analytical method outlined here has the potential to be applied to various geometries and incoming flow conditions, thereby offering a more comprehensive and immediate insight into vortex shedding and far-field noise. By determining the source location of each tonal noise, researchers and engineers can apply flow control and noise reduction methods more precisely.

ACKNOWLEDGMENTS

This work was partially supported by the National Natural Science Foundation of China (No.12072016, No.11772033).

CONFLICT OF INTEREST

The authors of the present study declare there is no conflict of interest to disclose.

AUTHORS CONTRIBUTION

Jiang Run-pei: Investigation, Data curation, Validation, Visualization, Writing - Original draft preparation. **Liu Pei-qing:** Conceptualization, Resources, Supervision, **Zhang Jin:** Methodology, Validation, Project administration, Writing - Reviewing and Editing. **Guo Hao:** Formal analysis.

REFERENCES

Afgan, I., Moulinec, C., Prosser, R., & Laurence, D. (2007). Large eddy simulation of turbulent flow for wall mounted cantilever cylinders of aspect ratio 6 and 10. *International Journal of Heat and Fluid Flow, 28*(4), 561–574. https://doi.org/10.1016/j.ijheatfluidflow.2007.04.014 .

Akkermans, R. A. D., Ewert, R. S., Moghadam, M. A., Dierke, J., & Buchmann, N. (2015). Overset DNS with application to sound source prediction. In S. Girimaji (Eds.), Notes on Numerical Fluid Mechanics and Multidisciplinary Design. (pp. 59-68). Springer. https://doi.org/10.1007/978-3-319-15141-0_4.

Ananthan, V. B., & Akkermans, R. A. D. (2023). Trailing edge noise reduction using bio-inspired finlets. *Journal of Sound and Vibration, 549*, 117553. https://doi.org/10.1016/j.jsv.2023.117553.

Ananthan, V. B., Akkermans, R. A. D., Hu, T., Liu, P. Q., & Rathje, N. (2022). Trailing-edge noise reduction potential of a locally applied shallow dimpled surface. *Journal of Sound and Vibration, 525*, 116745. https://doi.org/10.1016/j.jsv.2022.116745.

Ananthan, V. B., Bernicke, P., Akkermans, R. A. D., Hu, T., & Liu, P. Q. (2020). Effect of porous material on trailing edge sound sources of a lifting airfoil by zonal Overset-LES. *Journal of Sound and Vibration, 480*, 115386. https://doi.org/10.1016/j.jsv.2020.115386.

Ansys Inc. *ANSYS FLUENT* (version 2021R1) [Computer software]. https://www.ansys.com/resource-center/webinar/ansys-2021-r1-fluent-update.

Becker, S., Hahn, C., Kaltenbacher, M., & Lerch, R. (2008). Flow-induced sound of wall-mounted cylinders with different geometries. *AIAA Journal*, 46(9), 2265–2281. https://doi.org/10.2514/1.34865.

Bernicke, P., Akkermans, R. A. D., Ananthan, V. B., Ewert, R., Dierke, J., & Rossian, L. (2019). A zonal noise prediction method for trailing-edge noise with a porous model. *International Journal of Heat and Fluid Flow, 80*. 108469. https://doi.org/10.1016/j.ijheatfluidflow.2019.108469.

Bodling, A., & Sharma, A. (2019). Numerical investigation of low-noise airfoils inspired by the down coat of owls. *Bioinspir. Biomim. 14*, 016013. https://doi.org/10.1088/1748-3190/aaf19c.

Bourgeois, J. A., Noack, B. R., & Martinuzzi, R. J. (2013). Generalized phase average with applications to sensor-based flow estimation of the wall-mounted square cylinder wake. *Journal of Fluid Mechanics, 736*, 316. https://doi.org/10.1017/jfm.2013.494.

Bourgeois, J. A., Sattari, P., & Martinuzzi, R. J. (2011). Alternating half-loop shedding in the turbulent wake of a finite surface-mounted square cylinder with a thin boundary layer. *Physics of Fluids, 23*(9), 095101. https://doi.org/10.1063/1.3623463.

Cao, Y., Ping, H., Tamura, T., & Zhou, D. (2022). Wind peak pressures on a square-section cylinder: flow mechanism and standard/conditional POD analyses. *Journal of Wind Engineering and Industrial Aerodynamics, 222*, 104918 https://doi.org/10.1016/j.jweia.2022.104918.

Cao, Y., Tamura, T., & Kawai, H. (2019). Investigation of wall pressures and surface flow patterns on a wall-mounted square cylinder using very high-resolution Cartesian mesh. *Journal of Wind Engineering and Industrial Aerodynamics, 188*, 1–18. https://doi.org/10.1016/j. jweia.2019.02.013.

Chen, G., Li X., Sun, B., & Liang, X. (2022). Effect of incoming boundary layer thickness on the flow dynamics of a square finite wall-mounted cylinder. *Physics of Fluids*, 34, 015105. https://doi.org/10.1063/5.0076541.

Dawi, A. H., & Akkermans, R. A. D. (2018). Direct and integral noise computation of two square cylinders in tandem arrangement. *Journal of Sound and Vibration, 436*, 138–154. https://doi.org/10.1016/j.jsv.2018.09.008.

Duan, F., & Wang, J. J. (2021). Fluid–structure–sound interaction in noise reduction of a circular cylinder with flexible splitter plate. *Journal of Fluid Mechanics, 920*, A6. https://doi.org/10.1017/jfm.2021.403.

Frederich, O., Wassen, E., Thiele, F., Jensch, M., Brede, M., Huttmann, F., & Leder, A. (2008). *Numerical simulation of the flow around a finite cylinder with ground plate in comparison to experimental measurements.* [Conference session]. Contributions to the 15th STAB/DGLR Symposium, Darmstadt, Germany. https://doi.org/10.1007/978-3-540-74460-3_43

Geyer, T. F. (2020). Vortex shedding noise from finite, wall-mounted, circular cylinders Modified with Porous Material. *AIAA Journal 58*(5), 2019-2695. https://doi.org/10.2514/1.J058877.

Griffin, O. M. (1985). Vortex shedding from bluff bodies in a shear flow: a review. *Journal of Fluids Engineering, 107*, 298–306. https://doi.org/10.1115/1.3242481.

Hosseini, Z., Bourgeois, J. A., & Martinuzzi, R. J. (2013). Large-scale structure in dipole and quadrupole wake of a wall-mounted finite rectangular cylinder. *Experiments in Fluids, 54*(9) http://dx.doi.org/10.1007/s00348-013-1595-2.

Inoue, O., & Hatakeyama, N. (2002). Sound generation by a two-dimensional circular cylinder in a uniform flow. *Journal of Fluid Mechanics, 471*, 285-314. https://doi.org/10.1017/S0022112002002124.

Jeong, J., & Hussain, F. (1995). On the identification of a vortex. *Journal of Fluid Mechanics, 285*, 69–94. https://doi.org/10.1017/S0022112095000462.

Kadivar, E., Dawoodian, M., Lin, Y., & Moctar, O. (2024). Experiments on cavitation control around a cylinder using biomimetic riblets. *Journal of Marine Science and Engineering, 12*, 293. https://doi.org/10.3390/jmse12020293.

Kato, C., Iida, A., Takano, Y., Fujita, H., & Ikegawa, M. (1993). Numerical prediction of aerodynamic noise radiated from low Mach number turbulent wake, *AIAA-Paper*, 93-145. https://doi.org/10.2514/6.1993-145

Kawamura, T., Hiwada, M., Hibino, T., Mabuchi, I., & Kumada, M. (1984). Flow around a finite circular cylinder on a flat plate: cylinder height greater than turbulent boundary layer thickness. *Bulletin of JSME*, 27, 2142-2151. https://doi.org/10.1299/jsme1958.27.2142

Kim, W. W., & Menon, S. (1997, January). *Application of the localized dynamic subgrid-scale model to turbulent wall-bounded flows*. [Conference session] Technical Report AIAA-97-0210. 35th Aerospace Sciences Meeting, Reno, NV. American Institute of Aeronautics and Astronautics.

King, W. F., & Pfizenmaier, E. (2009). An experimental study of sound generated by flows around cylinders of different cross-section. *Journal of Sound and Vibration*, *328*(3), 318–337. https://doi.org/10.1016/j.jsv.2009.07.034.

Kitagawa, T., Fujina, Y., Kimura, K., & Mizuno, Y. (2002). Wind pressures measurement on end-cell-induced vibration of a cantilevered circular cylinder. *Journal of Wind Engineering and Industrial Aerodynamics*, *90*(4–5), 395–405, http://dx.doi.org/10.1016/S0167-6105(01)00200-8.

Krajnović, S. (2011). Flow around a tall finite cylinder explored by large eddy simulation. *Journal of Fluid Mechanics*, *676*, 294–317. https://doi.org/10.1017/S0022112011000450.

Kitagawa, T., Fujino, Y., & Kimura, K. (1999). Effects of free-end condition on end-cell-induced vibration. *Journal of Fluids and Structures*, *13*(4), 499-518. https://doi.org/10.1006/jfls.1999.0214.

Lee, C. W. (1997). Wake structure behind a circular cylinder with a free end. [Conference session] Proceedings of the 35th Heat Transfer and Fluid Mechanics Institute, Sacramento, CA. Heat Transfer and Fluid Mechanics Institute California State University, *35*, 241–251.

Lenz, B., Magalhaes, J. F., & Suh S. (2019). Numerical simulation of flow-induced sound from a wall-mounted finite length cylinder. *The Journal of the Acoustical Society of America*, *146*(4), 2838–2838. https://doi.org/10.1121/1.5136838.

Luo, S. C. (1993). *Flow past a finite length circular cylinder*. [Conference session]. Third International Offshore and Polar Engineering Conference.

Maryami, R., & Liu, Y. (2024). Cylinder flow and noise control by active base blowing. *Journal of Fluid Mechanics*, *985*, A10. https://doi.org/10.1017/jfm.2024.261.

Maryami, R., Arcondoulis, E. J. G., Guo, J., & Liu, Y. (2024). Experimental investigation of active local blowing on the aerodynamic noise reduction of a circular cylinder. *Journal of Sound and Vibration*, *578*, 118360. https://doi.org/10.1016/j.jsv.2024.118360.

Moradi, M. A., & Mojra, A. (2024). Flow and noise control of a cylinder using grooves filled with porous material. *Physics of Fluids*, *36*, 045133. https://doi.org/10.1063/5.0205125.

Moreau, D. J., & Doolan, C. J. (2013). Flow-induced sound of wall-mounted finite length cylinders. *AIAA Journal*, *51*(10), 2493–2502. https://doi.org/10.2514/1.J052391.

Noack, B. R. (1991). On cell formation in vortex streets. *Journal of Fluid Mechanics*, 227, 293-308. https://doi.org/10.1017/S0022112091000125.

Park, C. W., & Lee, S. J. (2000). Free end effects on the near wake flow structure behind a finite circular cylinder. *Journal of Wind Engineering and Industrial Aerodynamics*, *88*(2-3), 231-246. https://doi.org/10.1016/S0167-6105(00)00051-9.

Park, C. W., & Lee, S. J. (2002). Flow structure around a finite circular cylinder embedded in various atmospheric boundary layers. *Fluid Dynamics Research*, *30*(4), 197-215. https://doi.org/10.1016/S0169-5983(02)00037-0.

Park, C. W., & Lee, S. J. (2004). Effects of free-end corner shape on flow structure around a finite cylinder. *Journal of Fluids and Structures*, *19*(2), 141–158. https://doi.org/10.1016/j. jfluidstructs. 2003.12.001.

Pattenden, R. J., Turnock, S. R., & Zhang, X. (2005). Measurements of the flow over a low-aspect-ratio cylinder mounted on a ground plane. *Experiments in Fluids*, *39*(1),10–21. http://dx.doi.org/10.1007/s00348-005-0949-9.

Porteous, R., Moreau, D. J., & Doolan, C. J. (2014). A review of flow-induced noise from finite wall-mounted cylinders. *Journal of Fluids and Structures*, *51*, 240–254. https://doi.org/10.1016/j.jfluidstructs.2014.08.012.

Porteous, R., Moreau, D. J., & Doolan, C. J. (2017). The aeroacoustics of finite wall-mounted square cylinders. *Journal of Fluid Mechanics*, *832*, 287–328. https://doi.org/10.1017/jfm.2017.682.

Qin, D., Li, T., Zhang, J. & Zhou, N. (2023). Numerical study on aerodynamic drag and noise of high-speed pantograph by introducing spanwise waviness. *Engineering Applications of Computational Fluid Mechanics*, *17*, 1, 2260463. https://doi.org/10.1080/19942060.2023.2260463.

Saeedi, M., & Wang, B .C. (2016). Large-eddy simulation of turbulent flow around a finite-height wall-mounted square cylinder within a thin boundary layer. *Flow, Turbulence and Combustion*, *97*(2), 513–538. https://doi.org/10.1007/s10494-015-9700-7.

Sakamoto, H., & Arie, M. (1983). Vortex shedding from a rectangular prism and a circular cylinder placed vertically in a turbulent boundary layer. *Journal of Fluid Mechanics*, 126, 147–165. https://doi.org/10.1017/S0022112083000087.

Sattari, P., Bourgeois, J. A., & Martinuzzi, R. J. (2012). On the vortex dynamics in the wake of a finite surface-mounted square cylinder. *Experiments in Fluids*, *52*(5), 1149–1167. https://doi.org/10.1007/s00348-011-1244-6

Seo, J. H., & Moon, Y. J. (2007). Aerodynamic noise prediction for long-span bodies. *Journal of Sound and Vibration*, *306*(3-5), 564-579. https://doi.org/10.1016/j.jsv.2007.05.042.

Sumner, D., Heseltine J. L., & Dansereau O. J. P. (2004). Wake structure of a finite circular cylinder of small

aspect ratio. *Experiments in Fluids*, 37, 720. http://dx.doi.org/10.1007/s00348-004-0862-7.

Wang, C. H., & Li, Y. (2023). Control of a circular cylinder flow using attached solid/perforated splitter plates at deflection angles. *Physics of Fluids*, *35*, 105109. https://doi.org/10.1063/5.0165632.

Wang, H. F., & Zhou, Y. (2009). The finite-length square cylinder near wake. *Journal of Fluid Mechanics*, 638: 453–490. https://doi.org/10.1017/S0022112009990693.

Wang, H. F., Zhou, Y., Chan, C. K., & Lam, K. S. (2006). Effect of initial conditions on interaction between a boundary layer and a wall-mounted finite-length-cylinder wake. *Physics of Fluids*, 18(6), 561 https://doi.org/10.1063/1.2212329.

Xiao, C., & Tong F. (2023). Experiment on noise reduction of a wavy cylinder with a large spanwise wavelength and large aspect ratio in aeroacoustic wind tunnels. *Applied Sciences*, *13*, 6061. https://doi.org/10.3390/app13106061.

Yauwenas, Y., Porteous, R., Moreau, D. J., & Doolan, C. J. (2019). The effect of aspect ratio on the wake structure of finite wall-mounted square cylinders. *Journal of Fluid Mechanics*, 875, 929-960. https://doi.org/10.1017/ jfm.2019.522.

Zheng, C. T., Zhou, P., Zhong, S. Y., & Zhang, X. (2023). Experimental investigation on cylinder noise and its reductions by identifying aerodynamic sound sources in flow fields. *Physics of Fluids*, *35*, 035103. https://doi.org/10.1063/5.0138080.